Non-premixed combustion in rotary kilns using OpenFOAM: the effect of conjugate heat transfer and external radiative heat loss on the reacting flow and the wall

El Abbassi, M.; Dimas Ramadhan Abdillah Fikri, Dimas; Lahaye, D.J.P.; Vuik, Cornelis

DOI
10.1615/THMT-18.1290

Publication date
2018

Document Version
Final published version

Citation (APA)
El Abbassi, M., Dimas Ramadhan Abdillah Fikri, D., Lahaye, D. J. P., & Vuik, C. (2018). *Non-premixed combustion in rotary kilns using OpenFOAM: the effect of conjugate heat transfer and external radiative heat loss on the reacting flow and the wall*. 1121-1131. https://doi.org/10.1615/THMT-18.1290

Turbulence, Heat and Mass Transfer 9

Non-premixed combustion in rotary kilns using OpenFOAM: the effect of conjugate heat transfer and external radiative heat loss on the reacting flow and the wall.

M. el Abbassi[1], D.R.A. Fikri[1], D.J.P. Lahaye[1], C. Vuik[1]

[1]*Delft Institute of Applied Mathematics, Delft University of Technology,*
Van Mourik Broekmanweg 6, 2628 XE Delft, the Netherlands. m.elabbassi@tudelft.nl

Abstract — The wish to reduce the environmental footprint and to enhance economic gains of rotary kilns pushes the numerical simulation of combustion to include conjugate heat transfer. In this paper we study the influence of the refractory wall and radiative heat loss to the ambient, on the combustion process of a reference kiln model. Numerical results show that the inclusion of the refractory lining and the external radiative heat loss allows the inner wall temperature distribution to vary, with 60 % difference between its minimum and maximum. This is in sharp contrast with models that assume a fixed temperature at the wall. Consequently the maximum inner wall temperature increases by more than 200 %, the maximum flame temperature by nearly 13 % and maximum freeboard gas temperature by up to 90 %. It is thus important to account for these effects when modeling rotary kilns.

1. Introduction

Rotary kilns are long, slightly tilted, cylindrical furnaces that are used in a wide range of material processing industries, such as cement production, waste treatment, and metallurgy. The primary role of this device is to gradually heat the material that is moving slowly from the cold end, towards the hot end where the burner is positioned [1].

The phenomena of turbulent flow, combustion and heat transfer occurring in the kiln are strongly coupled. The heat released by the turbulent flame is transferred towards the material and the refractory lining. The absorption, emission and reflection of radiative heat influence the flow of gases in the freeboard and the flame characteristics. Moreover, as rotary kilns usually stand outside, a significant amount of heat is lost to the environment. With the increased environmental awareness and growing demand in production, numerical simulation is ideally suited to find optimal solutions in reducing the pollutant formation and specific fuel consumption, while also achieving a desired heat distribution to improve the production rate.

Different aspects of the rotary kiln have been studied using commercial CFD packages. In [2] we see the benefits of flue gas recirculation during oxy-fuel combustion. [3] shows how to prevent ring formation by changing the air to gas ratio. [4] is a good example that shows how CFD can aid in the operation and design of a kiln to meet the specified requirements. However, the big difference with the previous two researches is that the influence of the refractory wall and heat loss to the environment is left out. In [5] this influence is shown to some extent, but lacks detail and quantification.

In this work, we follow the recommendation in [4] and extend their kiln model. Our target is to include the effect of the refractory wall and the ambient heat losses. We integrate the required physics in a solver by using the library of the open source CFD toolbox OpenFOAM-v4.1. We make use of the developed code multiRegionReactingFoam [6, 7] which couples the combustion utility of OpenFOAM with the conjugate heat transfer (CHT) utility. In addition we implement the Eddy Dissipation Model for the turbulence-chemistry interaction and a Robin boundary condition for the external heat loss.

The simulations are conducted in three steps. First, the model without lining and an imposed temperature on the wall is simulated. Next, the lining is added using the CHT formulation. Finally the radiative heat loss to the environment is included. The calculated temperatures and radiative heat fluxes in these three cases are compared and shown in the results.

2. Governing equations and numerical models

In the fluid domain, the Favre-averaged transport equations of mass, momentum, chemical species and sensible enthalpy [8] are respectively described by

$$\frac{\partial(\bar{\rho})}{\partial t} + \nabla \cdot (\bar{\rho}\widetilde{u}) = 0, \tag{1}$$

$$\frac{\partial(\bar{\rho}\widetilde{u})}{\partial t} + \nabla \cdot (\bar{\rho}\widetilde{u}\widetilde{u}) = -\nabla\bar{p} + \nabla \cdot \mu\nabla\widetilde{u} - \nabla \cdot \bar{\rho}\widetilde{u"u"}, \tag{2}$$

$$\frac{\partial(\bar{\rho}\widetilde{Y_\alpha})}{\partial t} + \nabla \cdot (\bar{\rho}\widetilde{u}\widetilde{Y_\alpha}) = \nabla \cdot \bar{\rho}\Gamma\nabla\widetilde{Y_\alpha} - \nabla \cdot \bar{\rho}\widetilde{Y_\alpha"u"} + \widetilde{R}_\alpha, \tag{3}$$

$$\frac{\partial(\bar{\rho}\widetilde{h})}{\partial t} + \nabla \cdot (\bar{\rho}\widetilde{u}\widetilde{h}) = \frac{D}{Dt}\bar{p} + \nabla \cdot \frac{\lambda}{c_p}\nabla\widetilde{h} - \nabla \cdot \bar{\rho}\widetilde{h"u"} + \widetilde{Q}_c + \widetilde{Q}_r, \tag{4}$$

where ρ is the density, u the velocity, p the pressure, μ the laminar dynamic viscosity, Y_α the species mass fraction of species α, Γ the species diffusion coefficient, R the reaction rate of species α, h the specific sensible enthalpy, λ the thermal conductivity and c_p the specific heat capacity at constant pressure. The heat source terms Q_c and Q_r are due to combustion and thermal radiation, respectively. The over-bar and tilde notations stand for the average values, while the double quotation marks denote the fluctuating components due to turbulence. Note that several source terms (such as body forces and viscous heating) are neglected.

For solid regions, only the energy transfer needs to be solved and therefore the equation of enthalpy for solids, which is the following heat equation, has to be added to the list of transport equations 1-4:

$$\frac{\partial(\bar{\rho}h)}{\partial t} = \nabla \cdot (\lambda\nabla T). \tag{5}$$

To couple the thermal energy transport between the fluid and solid domains, two important conditions are required at the interface of the domains to ensure continuity of both the temperature and heat flux:

$$T_{f,int} = T_{s,int} \tag{6}$$

and

$$\lambda_f \frac{\partial T_f}{\partial y}\bigg|_{int,y=+0} = \lambda_s \frac{\partial T_s}{\partial y}\bigg|_{int,y=-0}, \tag{7}$$

where the subscripts f, s and int respectively stand for fluid, solid and interface. y is the local coordinate normal to the solid. Unclosed terms appear in the transport equations of the fluid domain due to Favre averaging. These will be treated in this section, followed by the elaboration of the heat transfer at the interface.

2.1. Turbulence

The unknown Reynolds stresses (last term of equation 2) are solved by employing the Boussinesq hypothesis that is based on the assumption that in turbulent flows, the relation between the Reynolds stress and viscosity is similar to that of the stress tensor in laminar flows, but with increased (turbulent) viscosity:

$$-\nabla\cdot\bar{\rho}\widetilde{u_i"u_j"} = \mu_t\left(\frac{\partial u_i}{\partial x_j}+\frac{\partial u_j}{\partial x_i}\right)-\frac{2}{3}\left(\rho k+\mu_t\frac{\partial u_k}{\partial x_k}\right)\delta_{ij}, \tag{8}$$

where μ_t is the turbulent dynamic viscosity and k the turbulent kinetic energy. The Reynolds stresses are closed with the Realizable k-ϵ turbulence model [9]. In the validation of [4] the model showed to have the best fit with experimental data of a piloted turbulent diffusion flame. The model solves two additional transport equations: one for the turbulent kinetic energy k, and the other for its dissipation rate ϵ

$$\frac{\partial(\bar{\rho}k)}{\partial t}+\nabla\cdot(\bar{\rho}\widetilde{u}k) = \nabla\cdot\left[\left(\mu+\frac{\mu_t}{\theta_k}\right)\nabla k\right]+\mu_t\left(\frac{\partial u_i}{\partial x_j}\right)^2-\bar{\rho}\epsilon, \tag{9}$$

$$\frac{\partial(\bar{\rho}\epsilon)}{\partial t}+\nabla\cdot(\bar{\rho}\widetilde{u}\epsilon) = \nabla\cdot\left[\left(\mu+\frac{\mu_t}{\theta_\epsilon}\right)\nabla\epsilon\right]+\bar{\rho}c_1S\epsilon-\bar{\rho}c_2\frac{\epsilon^2}{k+\sqrt{\nu\epsilon}}, \tag{10}$$

where θ_k,θ_ϵ and c_2 are constants. S is the modulus of the mean strain rate tensor, defined as $S=\sqrt{2S_{ij}S_{ij}}$ and c_1 is a function of k, ϵ and S. Again, note that the effect of buoyancy and other source terms are neglected. With k and ϵ, the turbulent viscosity can be determined by the following relation:

$$\mu_t = \bar{\rho}c_\mu\frac{k^2}{\epsilon}, \tag{11}$$

where in the Realizable k-ϵ model, c_μ is a function of k, ϵ, the mean strain rate and the mean rotation rate. This is one of the major differences compared to the other k-ϵ models where c_μ is a constant.

The turbulent scalar fluxes $\bar{\rho}\widetilde{\phi"u"}$ for the scalar chemical species and scalar sensible enthalpy (both denoted as ϕ) are closed with the Gradient diffusion assumption

$$-\bar{\rho}\widetilde{\phi"u"} = \nabla\cdot(\Gamma_t\widetilde{\phi}), \tag{12}$$

where Γ_t is the turbulent diffusivity determined by (assuming Lewis number = 1) the turbulent viscosity μ_t and turbulent Prandtl number Pr_t:

$$\Gamma_t = \frac{\mu_t}{Pr_t}. \tag{13}$$

2.2. Combustion

For calculating the mean chemical source term $\widetilde{R}_\alpha$ we implement the Eddy Dissipation Model (EDM) of Magnussen and Hjertager [10] in the OpenFOAM library. The EDM is an attractive model due to its computational efficiency and reasonable accuracy. The rate of reaction is taken as the minimum of the three rates for fuel, oxidant and products

$$\widetilde{R}_\alpha = -A\bar{\rho}\frac{\epsilon}{k}min\left(\bar{Y}_F,\frac{\bar{Y}_O}{\nu},B\frac{\bar{Y}_P}{1+\nu}\right), \tag{14}$$

where A and B are user defined model constants that by default are respectively equal to 4 and 0.5, and ν is the stoichiometric coefficient. Being a 'mixed is burnt' model type, the EDM excludes the effects of chemical kinetics and is based on the aspects of combustion occurring at high Reynolds and Damköhler numbers [8]. Therefore, the underlying assumption for choosing this model is that in rotary kilns the combustion is indeed mainly controlled by turbulent mixing. The model is validated in [11] where it is shown that the flame temperatures are over-predicted, as can be expected from 1-step reaction mechanisms with infinitely fast reaction rates. However, the profiles are well captured. The over predictions can be reduced when radiation is included.

2.3. Energy

The thermal conductivity λ in the averaged transport of the specific sensible enthalpy (equation 4) is replaced by the effective conductivity λ_{eff}, which incorporates the unknown turbulent scalar flux. From equations 12 and 13, λ_{eff} is defined by the Standard and Realizable k-ϵ models as

$$\lambda_{eff} = \frac{\mu}{Pr} + \frac{\mu_t}{Pr_t}, \tag{15}$$

where the turbulent Prandtl number, from experimental data, has an average value of 0.85. The heat release due to combustion $\widetilde{Q_c}$ follows from the calculations of $\widetilde{R}_\alpha$

$$\widetilde{Q_c} = -\sum_{\alpha=1}^{N-1} \Delta h^o_{f,\alpha} \widetilde{R_\alpha}, \tag{16}$$

where $\Delta h^o_{f,\alpha}$ is the formation enthalpy of species α, and N is the total number of species, of which only nitrogen is considered chemically inert by the EDM.

2.4. Thermal radiation

To obtain the mean radiation source term $\widetilde{Q_r}$ for the enthalpy transport equation, we employ the P1 approximation in accordance with the previous work, which solves the following partial differential equation for a non-scattering medium

$$-\nabla \cdot \left(\frac{1}{3\kappa} \nabla G \right) = \kappa(4\sigma T^4 - G), \tag{17}$$

where the radiation source term appears on the LHS of the equation. G is the total incident radiation, κ is the absorption coefficient of the medium and σ is the Stefan–Boltzmann constant. The P1 approximation is subject to the following boundary condition of the third kind [12]

$$-\frac{1}{3\kappa} \mathbf{n} \cdot \nabla G = -\frac{\kappa_w}{2(2-\kappa_w)} (4\sigma T_w^4 - G_w). \tag{18}$$

In this work we assume absorption coefficients of 0.2 and 0.6 for respectively the gas mixture and the refractory material. Adding radiation to the problem alters the interface condition (equation 7) to

$$\lambda_{eff} \frac{\partial T_f}{\partial y}\bigg|_{int,y=+0} + q_{r,in} - q_{r,out} = \lambda_s \frac{\partial T_s}{\partial y}\bigg|_{int,y=-0}, \tag{19}$$

where $q_{r,in}$ is the incident radiative heat flux absorbed by the solid and $q_{r,out}$ is the reflected and emitted radiative heat flux leaving the solid.

2.5. Convective heat transfer

An idea to calculate the convective heat transfer in turbulent flows would be to replace λ_f in equation 7 with the effective conductivity λ_{eff}, and to solve the temperature at the wall adjacent cell. However, k-ϵ models do not account for wall dampening effects due to the no-slip condition. Normally in free stream flow, viscous stresses are negligible compared to Reynolds stresses. However, close to the wall, the wall shear stress dampens out the velocity fluctuations, and at the wall, where $\vec{u}_i$ = 0, the Reynolds stresses are also zero. This means that the total shear stress at the wall is due to the viscous contribution, which also causes the mean velocity profile at the boundary layer to be logarithmic. Even other two-equation turbulence models that do incorporate wall dampening are unable to predict this accurately, unless the grid near the wall is extremely refined to capture the very sharp velocity gradients and the complex three-dimensional flow near the wall. This would require a substantial increase in computational power to solve the resulting problem. An alternative is to apply wall functions that make use of the universal behavior of the flow near the wall [13]. Assuming that the flow behaves like a fully developed boundary layer, the gradients of both the velocity and temperature at the cells adjacent to the wall interface boundary can be well predicted without the need for extreme refinement near the wall.

2.5.1. Wall functions

The foundation of the standard wall functions comes from the 'Law of the wall' (or the log law), which states that the average velocity of the turbulent flow near the wall is proportional to the logarithm of the normal distance from the wall. The log law was first published by von Kármán and is governed by the following relation

$$u^+ = \frac{1}{K}\ln(Ey^+), \tag{20}$$

where the constant K is known as the Von Kármán constant and, based on experiments, is equal to $K \approx 0.41$. The wall roughness parameter E is equal to $E \approx 9.8$ for smooth walls, and for rough walls other values can be assigned. y^+ is the non-dimensional normal distance from the wall and u^+ is the non-dimensional velocity parallel to the wall, determined by

$$y^+ = \frac{yu_\tau}{\nu} \qquad u^+ = \frac{u}{u_\tau} \qquad u_\tau = \sqrt{\frac{\tau_w}{\bar{\rho}}}, \tag{21}$$

where u_τ is the friction velocity and τ_w is the wall shear stress. By making use of the log law, it can be derived that (see e.g. [14], [15]) the kinetic energy and energy dissipation at the wall adjacent cells can be found with the following relations

$$k_P = \frac{u_\tau^2}{\sqrt{c_\mu}} \qquad \epsilon_P = \frac{u_\tau^3}{Ky}, \tag{22}$$

where the subscript P denotes the cell node coordinate adjacent to the wall. Using equations 11 and 15, μ_t and λ_{eff} in the boundary layer can also be found.

3. Problem setup

3.1. Geometry and boundary conditions

Two rotary kiln geometries with their dimensions can be found in [4], of which the so-called 'case A' geometry is selected. In this theoretical full scale kiln, the fuel methane enters from a

circular pipe at the burner head, while the primary air is supplied around the fuel in an annular shaped channel. The secondary air enters around the burner throughout the cross-section of the kiln. Since the kiln is modeled with steady-state RANS simulations and the flow is (statistically) symmetric, the kiln geometry is reduced to a 2D axisymmetric model. The mesh at the first 5 meter section of the kiln is shown in Fig. 1, where the refinement at the burner and at the lining can be seen. The mesh consists of 46.263 control volumes of which the solution is grid independent. The boundary conditions for the case of 10 MW are shown in table 1. The mass flow rates are calculated from the given power which is based on the fuel input. The air excess ratio of 1.12 is considered, of which 10% of the air enters as primary air. For the 40 MW case, the mass flow rates are quadrupled. The wall dimensions and properties are shown in Table 2.

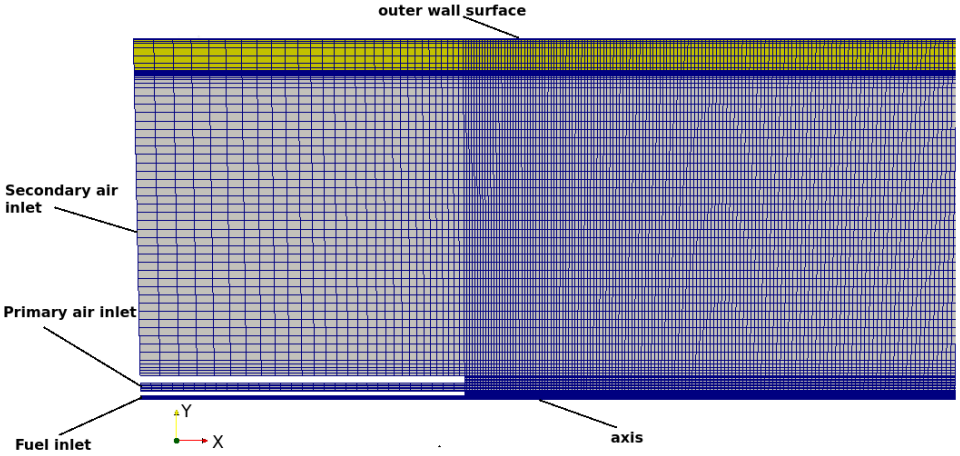

Figure 1: First 5 m section of the axisymmetric mesh of the kiln's freeboard region (gray) and 0.2 m thick refractory wall (yellow).

Table 1: Boundary conditions for the kiln model (10 MW). zG stands for the Neumann boundary condition zeroGradient. The patch normal mass flow rates are expressed in kg/s, and the temperatures in K. Species are denoted in mass fractions.

Variable	Fuel jet	Primary air	Secondary air	Gas-wall interface	Outer wall surface
$\dot{m}$	0.2	0.3896	3.5061	0	-
T	293	293	523	523/Coupled*	523*/$q_{r,ext}$**
Y_{CH_4}	1	0	0	zG	-
Y_{O_2}	0	0.23	0.23	zG	-
Y_{N_2}	0	0.77	0.77	zG	-

*Lining is included. **Lining and external heat loss is included.

Table 2: Thermal properties of the refractory material.

Density ρ	Thermal conductivity λ_s	specific heat capacity c_p	emissivity κ_s
$2800\,\mathrm{kgm^{-3}}$	$2.1\,\mathrm{Wm^{-1}K^{-1}}$	$860\,\mathrm{Jkg^{-1}K^{-1}}$	$0.6\,\mathrm{m^{-1}}$

3.2. External heat loss

In order to have a more realistic thermal boundary condition at the outer wall surface, we incorporate heat loss to the environment by introducing a Robin boundary condition on the outer wall surface. It is assumed that there is no wind so that heat loss due to forced convection can be neglected (note that there is freedom to incorporate this as well, using the convective heat transfer coefficient). Referring to Fig. 2, the radiative heat loss is calculated as follows.

The inner wall temperature at y=0 is known and defined as $T_{w,is}$.

$$T|_{y=0} = T_{w,is}. \tag{23}$$

At the outer wall surface (y=1) we use the Stefan-Boltzmann law to determine the flux, so that

$$\lambda_s \frac{\partial T}{\partial y}\bigg|_{y=1} = q_{r,ext} = \epsilon\sigma(T_{w,os}^4 - T_\infty^4), \tag{24}$$

where T_∞ is the ambient temperature which is set to 288,15 K (ISA). Using equations 23 and 24, it can be derived that the outer wall surface temperature

$$T_{w,os} = \frac{\epsilon\sigma}{\lambda_s}(T_{w,os}^4 - T_\infty^4)y_1 + T_{w,is}, \tag{25}$$

where y_1 is equal to the thickness of the refractory wall.

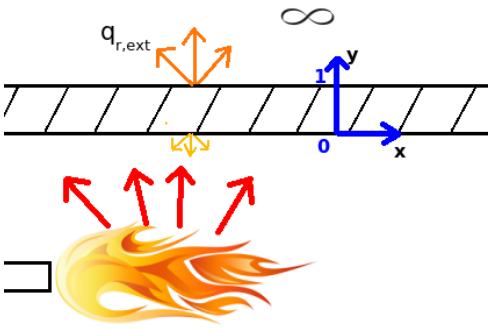

Figure 2: Picture of a confined turbulent flame with radiative heat loss to the environment.

3.3. Case studies

Three cases are studied in our work. In the first case, both the 10 MW and the 40 MW operating conditions are modeled, and the simulations are repeated with ANSYS-Fluent for verification. In the second case, the refractory lining is added and the constant wall temperature of 523 K is now shifted to the outer surface of the lining ($T_{w,os}$ = 523 K). In the last case, the external radiative heat flux $q_{r,ext}$ is incorporated and $T_{w,os}$ is defined by equation 25.

4. Results and discussion

4.1. Case 1: verification

In figure 3 the stream patterns and temperature contour plots are shown both with OpenFOAM-v4.1 and Fluent. The figure shows a typical Craya-Curtet flow under the condition where the momentum ratio of the central jet to the co-axial flow exceeds the critical value where the entrainment demands of the jet cannot be satisfied by the coflow, and an annular recirculation zone

forms at the wall [16]. Both solvers agree on the maximum temperature and overall temperature distribution. We do see a small difference in both the ignition delay and the total length of the reaction zone (see also Fig. 5). From the aerodynamics perspective, there is also good agreement in the flow field, with small discrepancy in the location of the recirculation zone. Overall, the results are very similar.

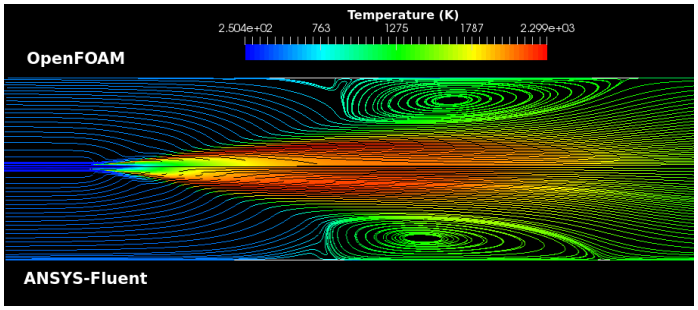

Figure 3: Comparison of the stream patterns and temperature at the first 16m section of the kiln. 40 MW.

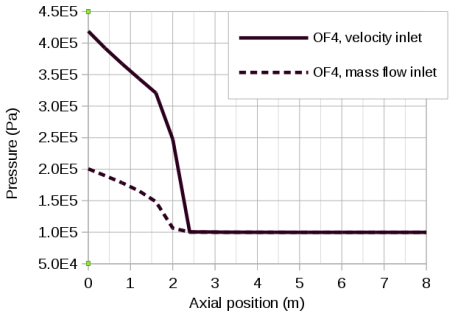

Figure 4: Progression of pressure along the central axis. 40 MW.

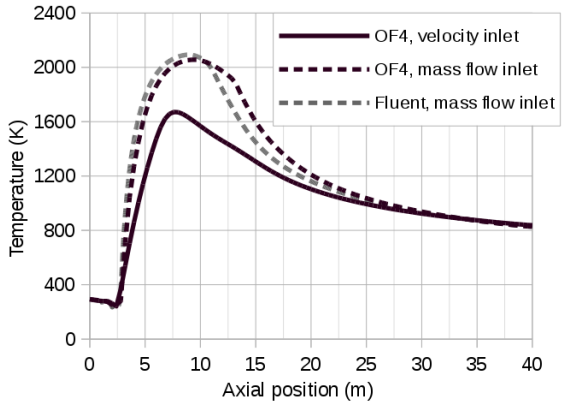

Figure 5: Temperature along the central axis in OpenFOAM-v4.1 and Fluent. 40 MW

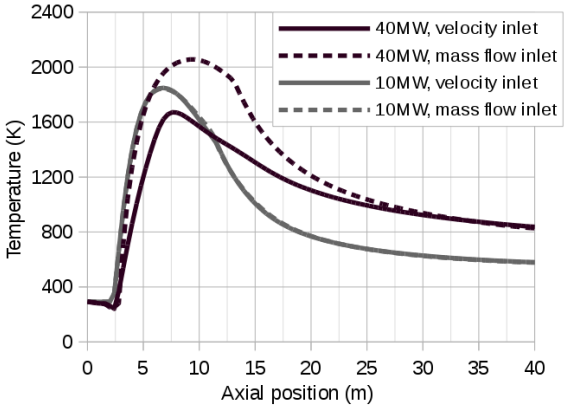

Figure 6: Temperature along the central axis in OpenFOAM-v4.1. 10 vs 40 MW.

4.1.1. High speed flow effects on inlet channel

When modeling the 40 MW case, prescribing a constant velocity inlet will lead to inaccurate results. A hand calculation of the velocity of the fuel (assuming a pressure of 1 atm) will lead to an inlet speed of nearly Mach 1.6. In practice this will cause the flow to become choked as the fuel inlet channel acts as a nozzle due to the increasing boundary layer thickness, and where the throat is to be expected at the end of the fuel channel. To overcome the choked condition, the required mass flow rate can only be achieved when the pressure upstream of the throat is increased [17], as can be seen in Fig. 4. Keeping the velocity constant at the inlet will lead to an almost twice as high fuel mass flow rate and therefore the reacting mixture becomes fuel rich. Fig. 5 shows that a prescribed velocity inlet will lead to a similar narrow peak as in [4], while using a mass flow inlet leads to a higher and broader peak temperature. Prescribing a mass flow inlet ensures mass conservation.

As for the 10 MW case, the fuel inlet speed is nearly at Mach 0.4 and therefore the flow is almost incompressible, leading to similar results between a velocity inlet and mass flow inlet (see Fig. 6)

4.2. Case 2: influence of the refractory wall

All of the following simulations are done with the 10 MW power configuration. Fig. 7 - 9 show the significant thermal effects on the gas domain when incorporating the refractory material. The lining provides insulation and leads to a much higher gas temperature (Fig. 7), with an increase of 10-90 % at the kiln's central axis. Also the maximum flame temperature increases with about 12 %, from 2267 K to 2548 K.

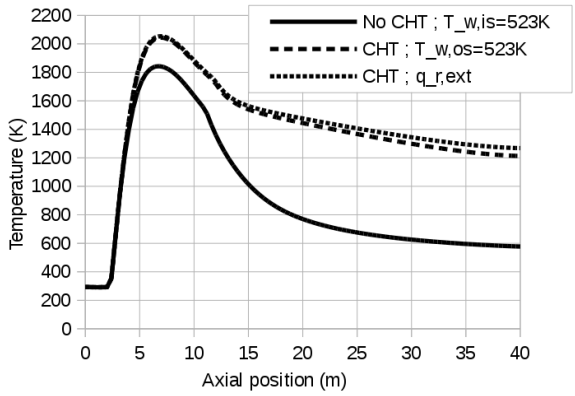

Figure 7: Temperature progression along the central axis. 10 MW.

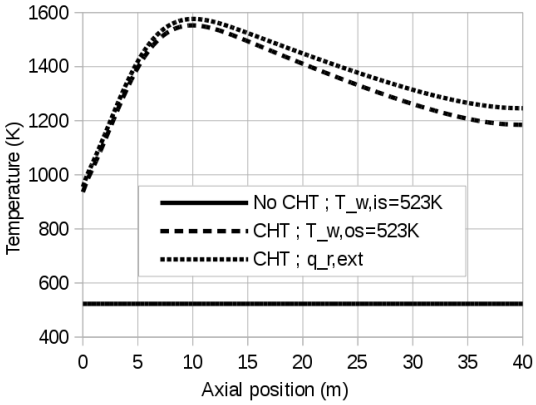

Figure 8: Temperature progression along the lining's inner surface. 10 MW.

The inner surface of the lining shows a parabolic temperature distribution of which the maximum temperature is increased almost three-fold (Fig. 8), with 60 % difference between its minimum and maximum. This is in sharp contrast with assuming a fixed temperature at the wall, even if it is scaled up. Due to the lower temperature difference between the flame and the wall, the peak radiative heat flux to the wall decreases with nearly 80% as compared to a constant wall temperature of 523 K (Fig. 9). Although the numbers seem drastic so far, they reduce with a better estimation of a constant wall temperature. Nevertheless, the inaccuracies of assigning a constant temperature cannot be neglected.

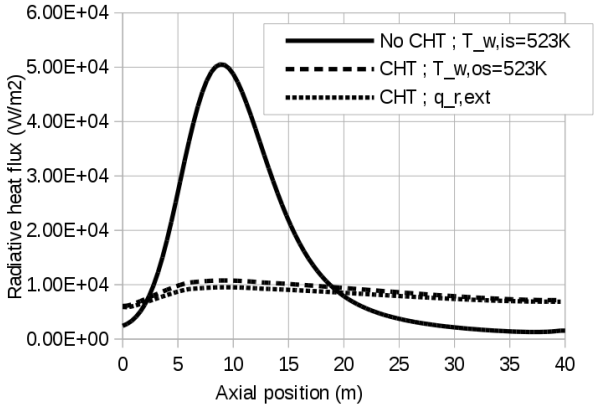

Figure 9: Radiative heat flux progression along the lining's inner surface. 10 MW.

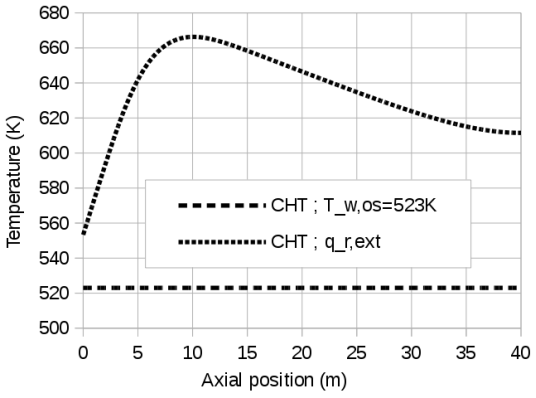

Figure 10: Temperature progression along the lining's outer surface. 10 MW.

4.3. Case 3: influence of external heat loss

When incorporating radiative heat loss to the environment, we also see a parabolic temperature distribution at the outer wall surface, with a maximum temperature increase of nearly 30 % (Fig. 10). In the gas domain however the effects are small (Fig. 7 - 9). This is due to the high thermal resistance of the refractory, in which the thermal effects of one side of the wall doesn't translate immediately to the other side. However, the influence on the gas domain is not insignificant; both the temperatures of the gas and inner wall surface increase with nearly 60 K at the outlet, and the maximum flame temperature increases with 18 K.

5. Conclusions

The aim of our work is to show the importance of including the energy transport in the refractory lining, and the external heat loss. Compared with the reference model where a constant temperature is assigned to the wall, our model predicts a temperature increase of 10 - 90 % throughout the central axis of the kiln. Our results show a parabolic temperature distribution at the inner wall surface, with more than 200 % increase of the peak temperature and 60 % difference between the mimimum and maximum. Due to the increased thermal insulation, we see that the maximum flame temperature increases with 12 %, and the maximum radiative heat flux to the wall decreases with 80 %. The inclusion of external radiative heat loss causes the outer wall surface temperature to increase with 30 %, whereas the effects on the inside of the kiln are much smaller. We succeeded in including more of the relevant physics in the kiln model by using OpenFOAM.

The results will improve when using more advanced submodels than the ones that have been chosen in our work, for which more research is needed. Moreover, the simulations were conducted on a non-rotating and empty rotary kiln. It is therefore also recommended to include the feedstock in the kiln model and allow the kiln to rotate in future researches.

As a final remark, specifically for channel flows, we stress the importance of applying a mass flow rate at the inlet boundaries when the flow cannot be considered incompressible, in order to ensure mass conservation at the inlets.

Acknowledgements

We would like to thank Eric Daymo from Tonkomo LLC for developing the solver multiRegionReactingFoam and for his collaboration on debugging the solver in order to make it more robust. We would also like to thank dr. Marco Talice for his support and for sharing his expertise.

References

[1] A.A. Boateng. *Rotary kilns: transport phenomena and transport processes.* Elsevier and Butterworth-Heinemann, Oxford, 2nd edition, 2016.

[2] D.A. Granados, F. Chejne, J.M. Mejía, C.A. Gómez, A. Berrío, and W.J. Jurado. Effect of flue gas recirculation during oxy-fuel combustion in a rotary cement kiln. *Energy*, 64:615–625, 2014.

[3] M. Pisaroni, R. Sadi, and D. Lahaye. Counteracting ring formation in rotary kilns. *Journal of Mathematics in Industry*, 2:3, 2012.

[4] H.F. Elattar, E. Specht, A. Fouda, and A.S Bin-Mahfouz. Study of parameters influencing fluid flow and wall hot spots in rotary kilns using cfd. *The Canadian Journal of Chemical Engineering*, 94:355–367, 2016.

[5] B. Manickam, F. Dinkelacker, T. Lobe, and M. Tertychnyy. Enriched oxygen combustion simulation for rotary kiln application. *4th European Combustion Meeting, Vienna*, 2009.

[6] Source code of chtMultiRegionReactingFoam. `https://github.com/TonkomoLLC`. accessed: 2017-01-15.

[7] E.A. Daymo and M. Hettel. Chemical reaction engineering with DUO and chtMultiRegionReactingFoam. 4th OpenFOAM User Conference 2016, Cologne-Germany, 2016.

[8] T. Poinsot and D. Veynante. *Theoretical and Numerical Combustion*. R.T. Edwards, Inc., Philadelphia, 2nd edition, 2005.

[9] T.H. Shih, W.W. Liou, A. Shabbir, Z. Yang, and J. Zhu. A new k-epsilon eddy-viscosity model for high Reynold number turbulent flows - model development and validation. *Computers & Fluids*, 24(3):227–238, 1995.

[10] B.F. Magnussen and B.H. Hjertager. On mathematical modeling of turbulent combustion with special emphasis on soot formation and combustion. *Symposium (International) on Combustion*, 16:719–729, 1977.

[11] H.I. Kassem, K.M. Saqr, H.S. Aly, M.M. Sies, and M. Abdul Wahid. Implementation of the eddy dissipation model of turbulent non-premixed combustion in OpenFOAM. *International Communications in Heat and Mass Transfer*, 38:363–367, 2011.

[12] M.F. Modest and D.C. Haworth. *Radiative Heat Transfer in Turbulent Combustion Systems, Theory and Applications*. Springer, Cham, 2016.

[13] H.K. Versteeg and W. Malalasekera. *An Introduction to Computational Fluid Dynamics: The Finite Volume Method*. Pearson Education Limited, Harlow, 2nd edition, 2007.

[14] H. Schlichting. *Boundary-layer Theory*. McGraw-Hill, New York, 7th edition, 1979.

[15] L. Davidson. *An Introduction to Turbulence Models*. Chalmers University of Technology, Department of Thermo and Fluid Dynamics, 2016.

[16] A. Revuelta, C. Martínez-Bazán, A. L. Sánchez, and A. Liñán. Laminar Craya–Curtet jets. *Physics of Fluids*, 16(1):208–211, 2004.

[17] J.D. Anderson, Jr. *Fundamentals of Aerodynamics*. McGraw-Hill, New York, 5th edition, 2011.